DUTKIEWICZ, J. & THOMAS, G. (1975). *Metall. Trans.* **6A**, 1919-1928.
FONTAINE, D. DE (1975). *Acta Metall.* **23**, 553-571.
FONTAINE, D. DE (1979). *Solid State Phys.* **34**, 73-274.
FURNROHR, P. (1976). PhD Thesis, Univ. of Stuttgart.
HIRAGA, K., HIRABAYASHI, M., TERASAKI, O. & WATANABE, D. (1982). *Acta Cryst.* A**38**, 269-274.
HIRAGA, K., SHINDO, D., HIRABAYASHI, M., TERASAKI, O. & WATANABE, D. (1980). *Acta Cryst.* B**36**, 2550-2554.
KESTERNICH, W., CARPENTER, R. W. & KENIK, E. A. (1982). *Metall. Trans.* **13A**, 213-219.
KHATCHATURYAN, A. G. (1973). *Phys. Status Solidi B*, **60**, 9-37.
MARTIN, P. L. (1982). PhD Thesis, Carnegie-Mellon Univ.
OKAMOTO, P. R. & THOMAS, G. (1971). *Acta Metall.* **19**, 825-841.
RUEDL, E., DELAVIGNETTE, P. & AMELINCKX, S. (1968). *Phys. Status Solidi*, **28**, 305-328.
SHINDO, D. (1982). *Acta Cryst.* A**38**, 310-317.
SPRUIELL, J. E. & STANSBURY, E. E. (1965). *J. Phys. Chem. Solids*, **26**, 811-822.
STOBBS, W. M. (1983). Private communication.
STOBBS, W. M. & CHEVALIER, J. P. A. A. (1978). *Acta Metall.* **26**, 233-240.
TERASAKI, O., WATANABE, D., HIRAGA, K., SHINDO, D. & HIRABAYASHI, M. (1980). *Micron*, **11**, 235-240.
THOMAS, G. & SINCLAIR, R. (1977). *Acta Metall.* **25**, 231-234.
VAN DYCK, D., VAN TENDELOO, G. & AMELINCKX, S. (1982). *Ultramicroscopy*, **10**, 263-280.
VAN TENDELOO, G. (1976). *Mater. Sci. Eng.* **26**, 209-220.
VAN TENDELOO, G. (1980). *J. Microsc.* **119**, 125-140.
VAN TENDELOO, G. & AMELINCKX, S. (1978). *Phys. Status Solidi A*, **47**, 555-564.
VAN TENDELOO, G. & AMELINCKX, S. (1981*a*). *Phys. Status Solidi A*, **65**, 73-86, 431-446.
VAN TENDELOO, G. & AMELINCKX, S. (1981*b*). *J. Microsc. Spectrosc.* **6**, 371-382.
VAN TENDELOO, G. & AMELINCKX, S. (1983). *Phys. Status Solidi A*, **77**, K9-K11.
VAN TENDELOO, G., DE RIDDER, R. & AMELINCKX, S. (1978). *Phys. Status Solidi A*, **49**, 655-666.

Acta Cryst. (1985). B**41**, 292-298

An Investigation of a Metastable Form of GaS by Convergent-Beam Electron Diffraction and High-Resolution Electron Microscopy

BY P. GOODMAN, A. OLSEN* AND H. J. WHITFIELD

Division of Chemical Physics, CSIRO, Melbourne, Australia

(*Received* 27 *December* 1983; *accepted* 9 *April* 1985)

Abstract

GaS prepared at temperatures below that required for adequate annealing is found to yield microcrystals with a much higher stacking-fault density and correspondingly lower overall crystal symmetry than that found for hexagonal β-GaS. The results of a high-resolution electron-microscopy analysis suggest that this character is associated with the predominance in the material of a high-pressure modification of GaS, present metastably in the partially annealed sample. It is concluded that details of preparation, including final annealing, are important in determining the microscopic crystal structure, and that discrepancies which have been highlighted recently between single-crystal diffraction measurements and those carried out on bulk microcrystalline samples may largely be explained by differences in preparative technique.

I. Introduction

Convergent-beam electron diffraction has in the past been largely used for examination of highly perfect crystal regions, and its application to structural study of faulted materials has been relatively little exploited. The earlier analysis of β-GaS (Goodman & Whitfield, 1980) is a good example of CBED analysis of fault-free single-crystal regions. This phase is formed by high-temperature annealing, above 1173 K, and the macrocrystals are in the form of graphite-like sheets, with a ready micaceous cleavage.

However, several alternative methods have been used in preparing GaS for analysis, particularly when finely powdered samples are required, including one in which the annealing is carried out below 973 K. Material prepared in this way has been recently examined by Bastow, Campbell & Whitfield (1981) using nuclear quadrupole resonance (NQR). Their finding of a new characteristic NQR spectrum has added to the already considerable debate about the nature of structural variants occurring at room temperature and pressure. Since crystals from this preparation are characteristically too small for single-crystal X-ray diffraction, this appeared as an ideal project for joint study by CBED and high-resolution electron microscopy. A brief summary of previous investigation is given below.

* Permanent address: Department of Physics, University of Oslo, Norway.

0108-7681/85/050292-07$01.50

Survey of GaS *structure analysis*

GaS has a layer structure which is covalently bonded within the layers but which has only van der Waals forces, or weak Coulomb forces, acting between layers. The well established polytype, β-GaS, which is stable at room temperature and pressure, has the hexagonal space group $P6_3/mmc$, and unit-cell dimensions $a = 3{\cdot}585$, $c = 15{\cdot}50$ Å (Wyckoff, 1963). The two layers of the structure are related by a 180° rotation, and the high disinclination for stacking faulting (Basinsky, Dove & Mooser, 1963) has been attributed to the fact that, in this polytype, the neighbouring, puckered, layers are matched geometrically. Alternative stacking sequences which have been described for the ε and γ structures of GaSe (Kuhn, Chevy & Chevalier, 1975)* have sometimes been proposed for GaS samples of low symmetry, but in fact have never been identified in any GaS structure analysis. An early conclusion of van der Zeil, Meixner & Kasper (1973), based on optical second-harmonic observations, was that regions of lower symmetry appear within the β-phase matrix of GaS. This conclusion was not supported by later X-ray and electron diffraction single-crystal investigations by Kuhn & Chevy (1976) and by Goodman & Whitfield (1980), respectively, who found only the pure β phase. The latter authors were, however, using samples either grown by vapour transport, or annealed after preparation at high temperature (between 1173 and 1223 K), whereas van der Zeil *et al.* (1973) were working with a sample which was slowly cooled from the melt to room temperature.

d'Amour, Holzapfel, Polian & Chevy (1982), using single-crystal X-ray diffraction, recently found a new high-pressure structure for GaS, stable above 2·0 GPa. In this structure, alternate layers are related by rotation about the vertical Ga–Ga axis, so that all Ga atoms are aligned in a single column along [001] and the space group of the β phase, namely $P6_3/mmc$, is preserved. The ε polytype, on the other hand, has the lower symmery of $P\bar{6}m2$. The high-pressure structure (called 'HP' in this paper) can be derived from the β structure by displacements of the layers.

For the purpose of further discussions, the three polytypes being proposed for GaS, namely β, HP and ε, are shown diagramatically in Fig. 1, in [110] and [001] projections.

* It is worth pointing out here that in Table 1 of Kuhn *et al.* there is an error in the Se-atom positions allocated to the ε phase, which was originally correctly described by Schubert, Dörre & Kluge (1955). These should be located in the 2(i) and 2(h) positions of the space group $P\bar{6}m2$.

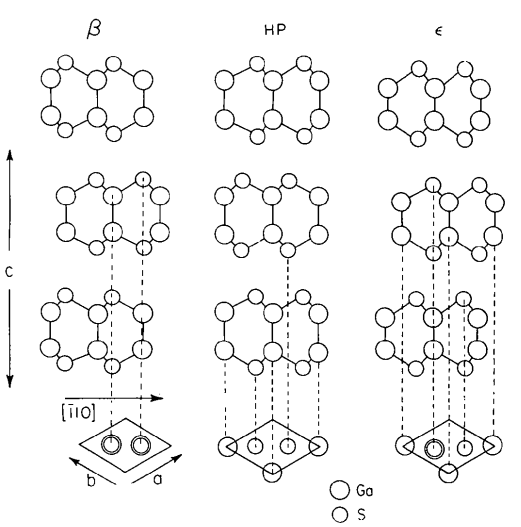

Fig. 1. Schematic representation of the three polytypes, β, HP, and ε, initially considered possible for GaS. The stacking sequence is seen in the [110] projections, shown in the main part of the figure. The [001] projections are shown directly below.

II. CBED analysis

(1) *Stacking-fault density analysis by CBED*

A simple way to investigate stacking disorder in a crystal is to examine the character of two-beam-like patterns, or few-beam patterns which are obtained from orientations of low symmetry (away from the principal zone axes). In these patterns a heavily faulted crystal will yield a CBED pattern with a high density of stacking-fault fringes, which are readily distinguished from perfect-crystal intensity modulations by their sharpness and high frequency and contrast. On the other hand, even a single stacking fault can cause a striking change to the normally expected diffracted-beam pattern; this will usually cause a marked asymmetry in the intensity distribution, for reflexions for which $\mathbf{R} \cdot \mathbf{g} \neq 0$ ($\mathbf{R}$ = the displacement vector; $\mathbf{g}$ = the diffraction vector). This effect is shown in Fig. 2, where results from a series of computations for a two-beam interaction obtained by analogue computation (Johnson, 1968) for crystals containing single and multiple stacking faults are shown. The diagrams in the top row, *A*, show that a single stacking fault placed near the crystal depth corresponding to an intensity maximum for the diffracted beam produces a marked effect (asymmetry) on the rocking curve. The last calculation, *B*, shows that with even higher fault densities, much more rapid, sharp, oscillations are produced.

Figs. 3(*a*) and 3(*b*) are CBED diffraction diagrams taken from different microcrystals of the new low-temperature-annealed GaS preparation, exhibiting a relatively low and high stacking fault density, respectively. Fig. 3(*a*) shows a single high-order reflexion excited directly, from a crystal with perhaps only one stacking fault, which would be sufficient to cause an asymmetric profile within the satisfied reflexion.

Fig. 3(*b*) shows a CBED pattern in which the few beams excited are covered by multiple stacking-fault fringes. This type of pattern typifies a heavily faulted crystal.

Stacking-fault fringes remain visible in satisfied reflexion discs even close to zone-axis orientations. However, at the exact zone axis when no zero-layer reflexions are satisfied this type of contrast is lost. The zone-axis patterns are needed to determine the overall crystal symmetry. By taking both sets of data therefore we obtain, in favourable circumstances, a semiquantitative analysis of stacking faulting.

(2) *Symmetry of CBED patterns*

Patterns were taken from the exact [001] zone axis from crystals of various thicknesses, which had been deposited directly onto supporting film from ethanol dispersions formed alternately by grinding the original sample under ethanol, and by simple agitation of the sample–ethanol mix using an ultrasonic bath. The patterns showed the common characteristic of having very weak first-order 100 reflexions and relatively strong 110 reflexions. This is in marked contrast to patterns previously obtained from the regularly stacked β phase in which the 100 reflexions are very much the strongest of the zone pattern, and many times more intense than the 110 set [see Fig. 6(*a*) of Goodman & Whitfield (1980)]. Fig. 4(*a*) is from a crystal of only a few unit cells thickness. Trigonality is present in the weak inner ring of reflexions; Fig. 4(*b*) from a thicker crystal shows this trigonality more clearly. Finally, Fig. 4(*c*) shows a zone pattern from a relatively thick region taken with a large diffraction aperture in order to show details within the strong 110-type discs. This pattern shows no exact symmetry, and is evidently from a heavily faulted crystal. Multiple diffraction, from non-aligned crystal domains, is evident from multiple-diffraction discs, and the lack of symmetry is attributable to the presence in the crystal of several faults which are not purely stacking faults.

Patterns were next taken in settings close to the [001] zone axis. With regard to whole-pattern symmetries, patterns taken with the incident beam within the [100] plane consistently showed a [100]* mirror line as in Fig. 5(*a*), whereas those taken with the incident beam within the [110] plane showed a lack of mirror symmetry across the [110]* line as seen by the intensity difference between the $1\bar{1}0$ and $\bar{1}00$ reflexions in Fig. 5(*b*). These observations are consistent with the trigonal symmetry found for the zone-axis patterns.

In the same pattern of Fig. 5(*b*) the directly excited high-order reflexion, with $\mathbf{g} = n \times [110]^*$, displays a

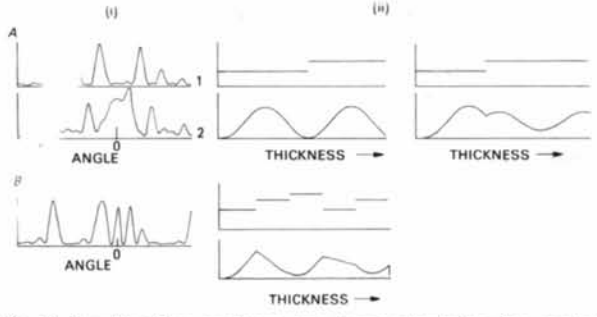

Fig. 2. Results of an analogue two-beam calculation for crystals containing stacking faults. Upper row, *A*: diagrams are for a single stacking fault in (1) a position of an extinction length and (2) of a half extinction length. Bottom row, *B*: diagrams are for multiple faults. Diagrams show (i) intensity plots as a function of angle (rocking curves), and (ii) stacking sequence as a function of crystal thickness: a horizontal line indicates a regular stacking sequence; steps up or down indicate positive or negative stacking-fault vectors occurring at a specific crystal depth. Immediately below each stacking-sequence plot is an intensity plot, or *Pendellösung*, calculated for that sequence from the two-beam equations.

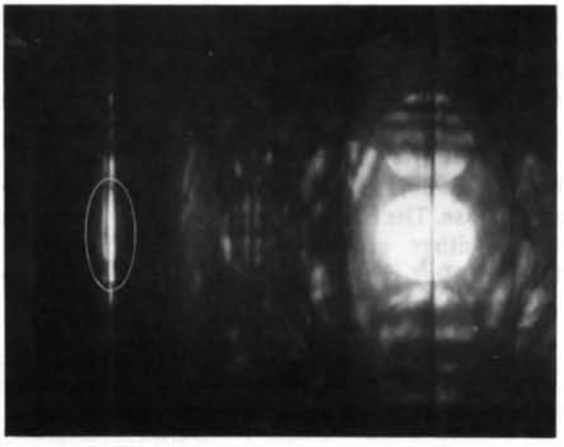

(*a*)

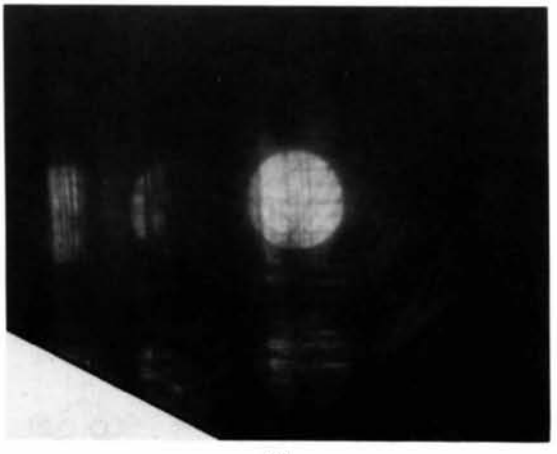

(*b*)

Fig. 3. CBED patterns taken at low-symmetry orientations. (*a*) An asymmetric *hkl* diffraction profile produced by at least one stacking fault having a displacement vector **R**, such that $\mathbf{R} \cdot \mathbf{g}_{hkl} \neq 0$. (*b*) Multiple-fringe fine structure produced by a crystal with a high stacking fault density.

symmetrical diffraction profile. This allows the deduction: $\mathbf{g} \cdot \mathbf{R} = 0$, and $\mathbf{R}$ is either zero or parallel to $[1\bar{1}0]^*$. Fig. 5(*c*), however, taken from the same crystal with a greater rotation away from the zone axis (so as to give a systematic-interaction row), shows an asymmetric profile for the satisfied $3\bar{3}0$ reflexion, indicating a finite displacement parallel to $[1\bar{1}0]^*$.

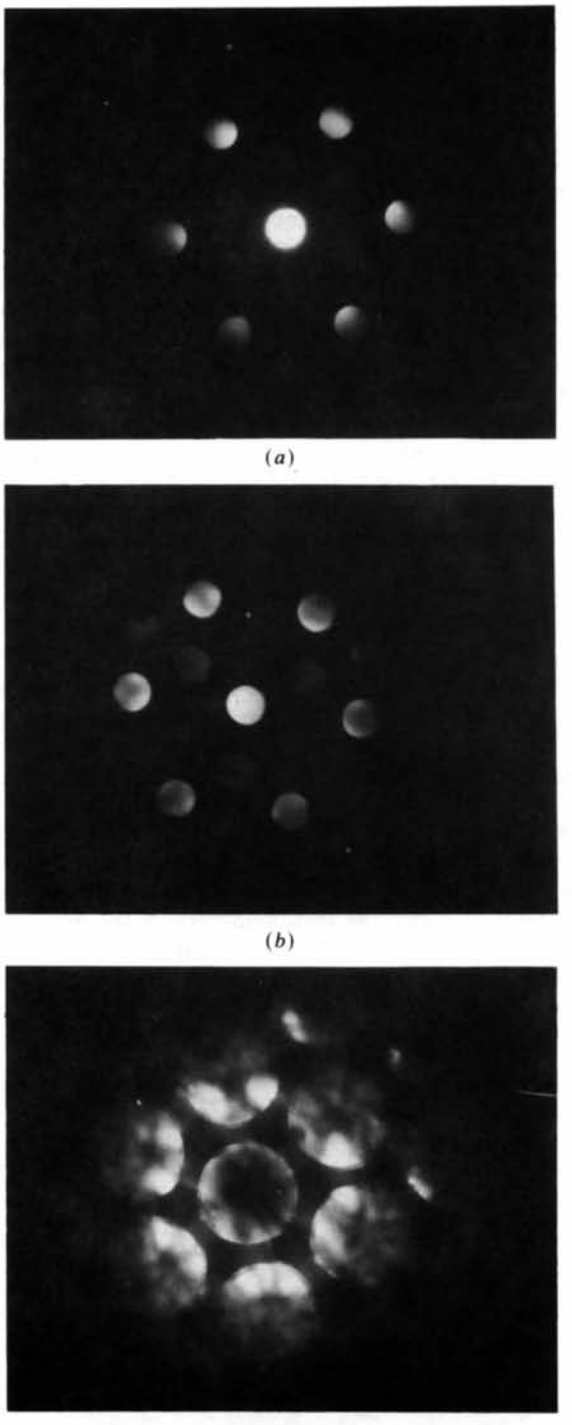

(*a*)

(*b*)

(*c*)

Fig. 4. (*a*) CBED [001] zone-axis pattern from a thin crystal of a few unit cells thickness. (*b*) CBED [001] zone-axis pattern from a thicker crystal, showing distinct trigonal symmetry. (*c*) Wide-aperture [001] zone-axis pattern from a thick crystal, showing no exact symmetry and multiple-diffraction effects.

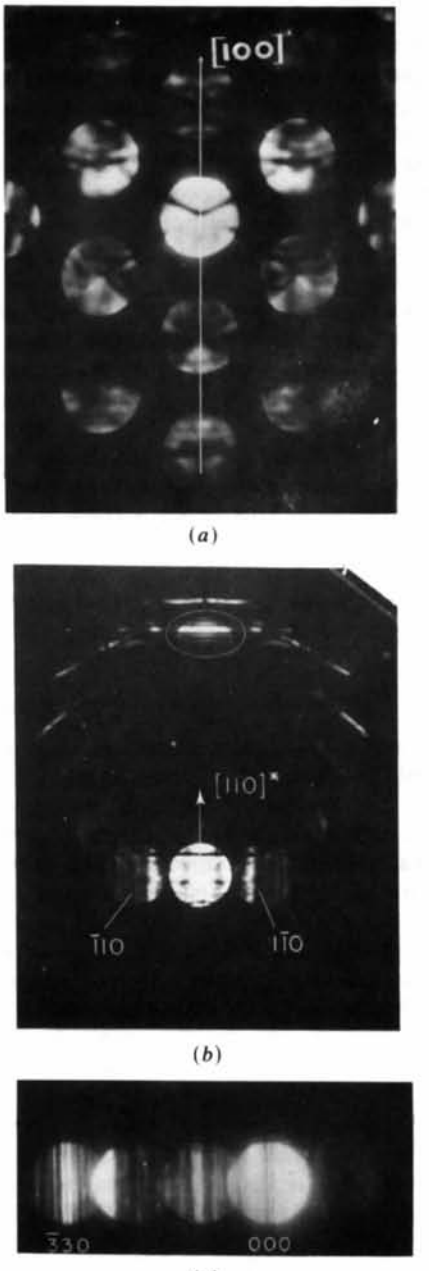

(*a*)

(*b*)

(*c*)

Fig. 5. (*a*) CBED pattern obtained from a setting close to the [001] zone axis, rotated so as to give a symmetrical setting with respect to the [100]* vector. (*b*) CBED pattern produced from same crystal as in (*a*), but with a rotation away from the zone so as to give a symmetrical setting with respect to the [100]* vector. Non-equivalent intensity regions in reflexions $\bar{1}10$ and $1\bar{1}0$ are indicated. (*c*) CBED pattern produced from the same crystal after further rotation away from the zone axis to produce a systematics-only pattern in which the $\bar{3}30$ reflexion is exactly excited.

(3) *Summary of diffraction evidence*

Trigonal symmetry together with a weak set of ⟨100⟩ reflexions is a characteristic of the CBED zone-axis patterns including even those from the thinnest regions. Further analysis, using good quality CBED patterns, indicates that these characteristics arise from crystals having stacking faults with the displacement vectors parallel to [1$\bar{1}$0], as is the case in graphite (Johnson, 1972). If all crystals of the sample have the same structure, then the same stacking-fault explanation must apply to the very thin regions. This is by no means an obvious or necessary assumption since one would expect the likelihood of stacking faulting to decrease with thickness unless there are some other factors involved. In considering the possible alternatives from known polymorphs, the ε-GaSe structure seems at first a possible candidate since it is trigonal in its unfaulted form. However, *N*-beam calculations show that an ε-GaS polytype would exhibit noticeable diffraction trigonality only at moderate thicknesses (*i.e.* greater than 50 Å) where the 110 reflexion is either weaker or of similar strength to the innermost 100-type reflexions. This model cannot therefore be fitted to the data.

It is concluded that graphitic-type stacking faulting is responsible for all the CBED characteristics found in the low-temperature-annealed sample.

III. High-resolution electron microscopy

Stacking sequence and structural arrangement within the unfaulted regions may be examined directly by means of high-resolution electron microscopy. For this, thin crystals cut approximately perpendicular to the natural [001] faces of the crystals had to be prepared. The sample was first centrifuged in a low-viscous epoxy resin, giving a dense and preferentially layered deposition. After polymerization at 313 K this was cut normal to the common (001) planes of the embedded deposit, using a diamond saw. The slices were polished by hand before ion-beam thinning from both sides. Optimum times for the final thinning were determined for the removal of mechanically damaged layers, and the production of crystal regions suitable for high-resolution imaging. The electron microscopy was carried out in a JEOL 200CX microscope fitted with a high-resolution pole piece ($C_s = 0{\cdot}95$ mm).

(1) *Identification of polytype*

A sample was found with several thin regions close to the [110] zone axis. Micrographs were taken with a negative defect of focus between −700 and −900 Å (maximum contrast). Fig. 6 shows a field from a crystal with an average [110] setting. Near the zone axis, the contrast is very sensitive to slight angular deviations, and to changes of crystal thickness, so that variations over the field are very apparent. Slight crystal curvature is often very useful in allowing the image to be scanned for regions of maximum symmetry, which are assumed to correspond to the zone setting. An initial examination of these micrographs indicated that, of the polytypes considered in Fig. 1, only the HP structure could give a qualitative match. This analysis assumed that at suitable negative defect of focus an intuitive interpretation down to a resolution of 2 Å could be applied (see also Moodie & Whitfield, 1983). The linear alignment of intramolecular tunnels of the structure image, parallel to the projected [001] direction, is a characteristic of large regions of the experimental micrographs (see, for example, upper left section of Fig. 6). This linear alignment is a feature of the HP structure in the [110] projection and not of either the β or ε structures which exhibit a zigzag alignment of molecular structure in that projection (see Fig. 1).

These preliminary indications were checked by *N*-beam lattice-image calculations. First of all, no image match could be obtained using the β structure. Computed images obtained from the HP structure reproduced the main experimental features remarkably well; finer image features reproduced in calculations are, however, lost experimentally. In detail, Figs. 7(*a*) and 7(*b*) show images computed for $\Delta f = -950$ Å at two neighbouring thicknesses, where holes in the structure show as white. The most obvious features of these computed images are the rows of white dots at half-unit-cell intervals. In comparing these with the image in the upper section of Fig. 6, the alignment of these white dots parallel to the [001] direction is reproduced, but the remaining intermolecular regions, which lack detail in the experiment, cannot be compared. By inspecting computed image Fig. 7(*b*) it is seen that the glide symmetry of the projected symmetry 'pmg' is determined by the interlayer image detail. If this is not resolved it is not possible to detect

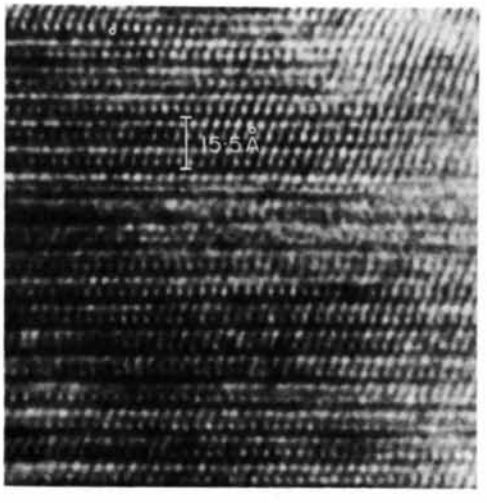

Fig. 6. Electron micrograph from the [110] orientation of GaS covering an extensive field.

readily the doubling of the c axis to 15·5 Å. This doubling is much more evident in the image from the slightly tilted crystal, computed in Fig. 7(c). Under these conditions ($\Delta f = -750$ Å) details linking the half unit cells appear with much more character, although the structure is no longer recognizable at this tilt.

In Fig. 8, a section of the experimental image is shown matched against this calculation (lower left), in a region which is tilted to the zone. The simulated image match shows that the weak lines linking the two halves of the unit cell are reproduced qualitatively. The structure is, however, more easily recognized from the less tilted parts of the image, at the upper right, where a scaled drawing of the projection is given for comparison.

The calculation of Fig. 7(c) corresponds to a tilt of 7 mrad from the zone axis. With greater tilt the image assumes the appearance of uniformly sloping rows (see upper left, Fig. 8) and again the two halves of the cell are indistinguishable at this resolution.

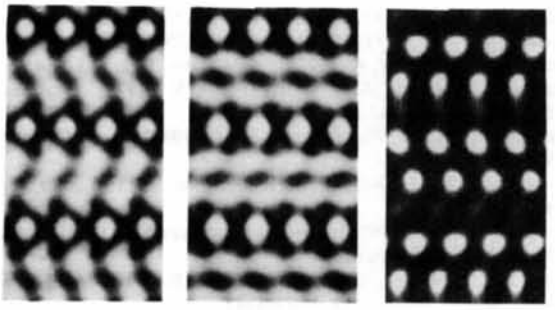

(a) (b) (c)

Fig. 7. N-beam computed images for the HP-GaS structure: (a) and (b): images computed for exact [110] zone, for $\Delta f = -950$ Å, at two thicknesses, H: (a) $H = 220$ Å; (b) $H = 180$ Å. (c) Computation for a crystal tilted 7 mrad to the [110] zone, with $\Delta f = -750$ Å, and $H = 220$ Å.

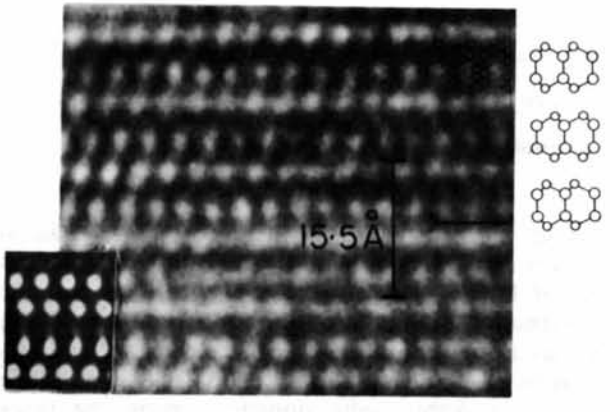

Fig. 8. A section of the [110]-zone image from a curved region of crystal taken at approximate $\Delta f = -800$ Å defocus. Inset upper right: a schematic alignment of three layers of the HP structure to the micrograph; micrograph region with vertically aligned 'molecular images' is bracketed; lower left: comparison with a one-unit-cell-deep section of the computed image of Fig. 7(c).

(2) *Stacking-fault analysis of images*

For the purpose of stacking-fault analysis, crystals may usefully be examined in off-axis settings. By tilting the GaS sample from the [110] setting so as to emphasize the $1\bar{1}2$ and 006 reflexions in the diffraction pattern, a very simple and high-contrast image is formed (see Fig. 9). Due to the diffraction asymmetry the unit-cell boundaries are no longer obvious, but the $[1\bar{1}0]$ structural rows are imaged (*cf.* Fig. 1), permitting a direct measurement of displacement vectors along this direction. As the crystal is rotated from the zone setting the four-row per unit cell appearance of the image is replaced by a characteristic three-row image seen in regions of Fig. 9, where a half unit cell is shown boxed [this rotation effect may be verified in the computed-images series: *e.g.* Fig. 7(c) represents a half-way step]. Fig. 9 shows a high density of stacking faults which separate small strain-free regions. Those regions marked $D1$ and $D2$ represent domains having the predominant hexagonal stacking sequence discussed above. $D2$ is displaced from $D1$ by the stacking fault $t1$, with a displacement vector $\mathbf{R} = \frac{2}{3}\mathbf{T}$ (or $-\frac{1}{3}\mathbf{T}$). $t2$ is a stacking fault in the reverse direction to $t1$ (with $\mathbf{R} = \frac{1}{3}\mathbf{T}$), returning the lattice to $D1$ registration. The displacement of $D2$ from $D1$ can readily be confirmed by laying a ruler along the imaged $1\bar{1}2$ rows. $t3$ represents two unit cells of A–B–C stacking. Since $\mathbf{T}$ can be identified directly with the $[1\bar{1}0]$ vector in the image of Fig. 9, $t1$ is identified as $\frac{1}{3}[1\bar{1}0]$.

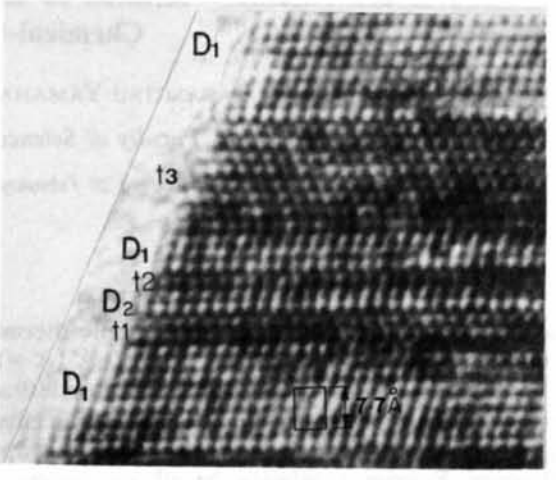

Fig. 9. Micrograph taken from a crystal setting near [110], to show stacking-fault contrast together with lattice resolution. Domains of the matrix lattice are marked as $D1$ and $D2$, while fault regions are indicated as $t1$, $t2$ and $t3$ (see text).

IV. Discussion

CBED [001] zone-axis patterns from thin crystals of this preparation are consistent with a stacking-faulted form of the hexagonal, $P6_3/mmc$, GaS structure, following the model found by Johnson (1972) for graphite. These patterns are, however, insensitive to the detailed host-lattice structure. High-resolution lattice images obtained from the [110] orientation provide the required complementary data. These images appear to be consistent only with a host lattice which has the HP-type stacking.

The crystal sizes and thicknesses of the CBED samples were much less than those used in the electron microscopy; however, the high density of stacking faults observed in both investigations suggests that faulting is a property of the bulk preparation, and contrasts with all reported observations made on well annealed β-GaS.

In the β phase, neighbouring kinked layers are matched geometrically, a feature which has been put forward as a principal reason for a disinclination for stacking faulting (Basinsky, Dove & Mooser, 1963). Such matching does not occur in the HP structure. If the latter were present in the preparation at room pressure and temperature, transformation to the β phase by means of stacking faulting would become energetically favoured, resulting in a reduction of the volume of HP phase present to small islands, metastably held by surrounding dislocations and stacking faults.

From our combined convergent-beam diffraction and high-resolution microscopy analysis we conclude that GaS annealed below 973 K still contains a proportion of HP-GaS in metastable form, interspersed with stacking faults.

This observation would explain the low stacking-fault energy associated with this sample, and should help to explain apparently conflicting conclusions drawn in the past concerning the structure of GaS, when a variety of preparation and annealing techniques have been used.

References

D'AMOUR, H., HOLZAPFEL, W. B., POLIAN, A. & CHEVY, A. (1982). *Solid State Commun.* **44**, 853-855.

BASINSKY, Z. S., DOVE, D. B. & MOOSER, E. (1963). *J. Appl. Phys.* **34**, 469-468.

BASTOW, T. F., CAMPBELL, I. D. & WHITFIELD, H. J. (1981). *Solid State Commun.* **39**, 307-311.

GARD, F. A. (1966). *Nature (London)*, **211**, 1078-1079.

GOODMAN, P. & WHITFIELD, H. J. (1980). *Acta Cryst.* A**36**, 219-228.

JOHNSON, A. W. S. (1968). *Acta Cryst.* A**24**, 534-543.

JOHNSON, A. W. S. (1972). *Acta Cryst.* A**28**, 89-91.

KUHN, A. & CHEVY, A. (1976). *Acta Cryst.* B**32**, 983-984.

KUHN, A., CHEVY, A. & CHEVALIER, R. (1975). *Phys. Status Solidi A*, **31**, 469-475.

MOODIE, A. F. & WHITFIELD, H. J. (1983). *Acta Cryst.* A**39**, 946-947.

SCHUBERT, K., DÖRRE, E. & KLUGE, M. (1955). *Acta Metall.* **46**, 216-224.

WYCKOFF, W. G. (1963). *Crystal Structures* Vol. 1, pp. 144-145. New York: Interscience.

ZEIL, J. P. VAN DER, MEIXNER, A. E. & KASPER, H. M. (1973). *Solid State Commun.* **12**, 1213-1215.

Acta Cryst. (1985). B**41**, 298-304

The Anharmonic Thermal Vibration in ZnX (X = S, Se, Te) and Its Dependence on the Chemical-Bond Characters

BY TAKAMITSU YAMANAKA AND MASAYASU TOKONAMI

Mineralogical Institute, Faculty of Science, University of Tokyo, Hongo, Tokyo 113, *Japan*

(*Received* 20 *February* 1985; *accepted* 22 *April* 1985)

Abstract

The X-ray diffraction study of anharmonic thermal vibration was carried out with respect to ZnX (X = S, Se, Te), having a zinc-blende structure, whose lattice-dynamical properties such as force constant and effective charge were determined by Raman spectroscopy. Difference Fourier syntheses based on harmonic refinements after correction of the diffraction intensities for thermal diffuse scattering exhibit a tetrapod shape of residual electron density around the Zn atoms, implying an anisotropy of the anharmonic thermal vibration. However, the residual density around the X atoms was subjected to influences of both the valence charge electrons and the anharmonic thermal vibration of the atoms. ZnTe, having a smaller interatomic force constant and less ionic bond character than ZnS and ZnSe, showed the most remarkable anharmonicity among the three compounds. The difference Fourier syntheses of ZnTe showed that the higher-order reflections indicated more salient anharmonicity and that the Zn atom has a larger anharmonic vibration than the Te atom. Cumulant expansion up to the fourth-rank tensors

0108-7681/85/050298-07$01.50